

Condensation and mixing in supernova ejecta

A.V. Fedkin^{a,*}, B.S. Meyer^b, L. Grossman^c

^a *Department of the Geophysical Sciences, The University of Chicago, 5734 South Ellis Ave., Chicago, IL 60637, USA*

^b *Department of Physics and Astronomy, Clemson University, Clemson, SC 29634, USA*

^c *Department of the Geophysical Sciences, and Enrico Fermi Institute, The University of Chicago, USA*

Received 24 August 2009; accepted in revised form 17 March 2010; available online 30 March 2010

Abstract

Low-density graphite spherules from the Murchison carbonaceous chondrite contain TiC grains and possess excess ^{28}Si and ^{44}Ca (from decay of short-lived ^{44}Ti). These and other isotopic anomalies indicate that such grains formed by condensation from mixtures of ejecta from the interior of a core-collapse supernova with those from the exterior. Using homogenized chemical and isotopic model compositions of the eight main burning zones as end-members, Travaglio et al. (1999) attempted to find mixtures whose isotopic compositions match those observed in the graphite spherules, subject to the condition that the atomic C/O ratio = 1. They were partially successful, but this chemical condition does not guarantee condensation of TiC at a higher temperature than graphite, which is indicated by the spherule textures. In the present work, model compositions of relatively thin layers of ejecta within the main burning zones computed by Rauscher et al. (2002) for Type II supernovae of 15, 21 and 25 M_{\odot} are used to construct mixtures whose chemical compositions cause equilibrium condensation of TiC at a higher temperature than graphite in an attempt to match the textures and isotopic compositions of the spherules simultaneously. The variation of pressure with temperature and the change in elemental abundances with time due to radioactive decay were taken into account in the condensation calculations. Layers were found within the main Ni, O/Ne, He/C and He/N zones that, when mixed together, simultaneously match the carbon, nitrogen and oxygen isotopic compositions, $^{44}\text{Ti}/^{48}\text{Ti}$ ratios and inferred initial $^{26}\text{Al}/^{27}\text{Al}$ ratios of the low-density graphite spherules, even at subsolar $^{12}\text{C}/^{13}\text{C}$ ratios. Due to the relatively large proportion of material from the Ni zone and the relative amounts of the two layers of the Ni zone required to meet these conditions, predicted ^{28}Si excesses are larger than observed in the low-density graphite spherules, and large negative $\delta^{46}\text{Ti}/^{48}\text{Ti}$, $\delta^{47}\text{Ti}/^{48}\text{Ti}$, $\delta^{49}\text{Ti}/^{48}\text{Ti}$ and $\delta^{50}\text{Ti}/^{48}\text{Ti}$ are produced, in contrast to the observed normal $\delta^{46}\text{Ti}/^{48}\text{Ti}$ and $\delta^{47}\text{Ti}/^{48}\text{Ti}$, large positive $\delta^{49}\text{Ti}/^{48}\text{Ti}$ and smaller positive $\delta^{50}\text{Ti}/^{48}\text{Ti}$. Although better matches to the observed $\delta^{46}\text{Ti}/^{48}\text{Ti}$, $\delta^{47}\text{Ti}/^{48}\text{Ti}$ and ^{28}Si excesses can be found using much smaller amounts of Ni zone material and some Si/S zone material, it is very difficult to match simultaneously the Ti and Si isotopic compositions in any mixtures of material from these deep layers with He/C and He/N zone material, regardless of the condensation sequence. The occurrence of Fe-rich, Si-poor metal grains inside the graphite spherules does not have a satisfactory explanation.

© 2010 Elsevier Ltd. All rights reserved.

1. INTRODUCTION

The ejecta from core-collapse supernovae (explosions of massive stars) vary in chemical and isotopic composition due to varying degrees of nuclear burning experienced during pre-explosion stellar evolution and explosive nucleo-

synthesis. In one-dimensional models, the ejecta are concentrically zoned in composition. It is common to divide the ejecta in one-dimensional models into eight zones marked by their most abundant isotope by mass (Meyer et al., 1995). As time passes after the explosion, the gaseous ejecta expand and cool, and condensation occurs as temperature falls. Equilibrium thermodynamic calculations (Lattimer et al., 1978; Sharp and Wasserburg, 1995; Ebel and Grossman, 2001; Lodders, 2006) have been used to predict the identities of condensates expected in supernova ejecta as

* Corresponding author. Tel.: +1 773 702 8131.

E-mail address: avf@uchicago.edu (A.V. Fedkin).

an aid to interpretation of textures and isotopic anomalies of presolar grains found in chondrites. Clayton et al. (1999) postulated that radiation-induced dissociation of $\text{CO}_{(\text{g})}$ would lead to condensation of carbon in supernova ejecta, but this was not based on experimental data and the authors did not consider the effect on the total condensation process in the likely event that all polyatomic species would be dissociated under such circumstances (Ebel and Grossman, 2001). Cherchneff and Dwek (2009) performed a theoretical study of the kinetics of formation and destruction processes of a large number of gaseous species in supernova ejecta. They concluded that molecular abundances do not reach steady state but they did not explore what condensate phases would be expected under these conditions. Nozawa et al. (2003) applied non-steady state nucleation and grain growth theory to the problem but predicted large abundances of minerals not seen among presolar grains from supernovae, such as SiO_2 , metallic Si, MgO, FeS and Fe_3O_4 , compared to some of those that have been seen, such as SiC, TiC, Al_2O_3 , MgAl_2O_4 and $\text{CaAl}_{12}\text{O}_{19}$ (Nittler et al., 2008). Thus, while kinetic effects accompanying formation of molecules and grains in supernova ejecta are undoubtedly important due to the rapid cooling and expansion of the gas and its interaction with ionizing radiation, rigorous kinetic treatment of condensation in such complex systems must await experimental study and/or a more advanced generation of theoretical investigations of rates along multiple chemical pathways. Equilibrium calculations provide a baseline for such treatments.

Spherules of low-density graphite are thought to have originated from core-collapse supernovae, due to excesses of ^{44}Ca and ^{41}K from decay of short-lived ^{44}Ti and ^{41}Ca , respectively, observed within them (Amari et al., 1996; Nittler et al., 1996) as well as correlation of the ^{44}Ti excesses with those of ^{28}Si , both of which are produced in the deep interiors of supernovae (Nittler et al., 1996; Amari and Zinner, 1997). Tiny inclusions of TiC were found inside the graphite by Nittler et al. (1996) and Bernatowicz et al. (1998, 1999), indicating that the TiC formed prior to the graphite. The ^{44}Ca is found in the TiC grains (Stadermann et al., 2005) and the ^{28}Si excesses are associated with the graphite (Bernatowicz et al., 1998). At equilibrium, condensation of graphite at a higher temperature than oxides can only occur in cosmic gases with atomic $\text{C/O} \geq 1$, a condition met in supernova ejecta only in carbon-rich zones that are widely separated from the inner Si-, Ti-rich zones by thick, intervening, O-rich zones. The presence of ^{44}Ti and ^{28}Si in graphite spherules implies that some material from the interior of the star must have been mixed with relatively large amounts of material from the C-rich outer zones compared to that from the intervening zones before graphite condensation. Using homogenized compositions of the main burning zones as end-members, Travaglio et al. (1999) tried to find mixtures whose isotopic compositions matched those measured in the low-density graphite while simultaneously satisfying the condition that $\text{C/O} = 1$. They partially succeeded in matching the isotopic compositions of the graphite spherules; however, the assumption that $\text{C/O} = 1$ does not guarantee condensation of TiC at a higher temperature than graphite, or at all.

In the present work, mixing models are constructed in an attempt to match the isotopic compositions of the low-density graphite spherules by relaxing one of Travaglio et al.'s (1999) constraints and modifying another. Specifically, instead of homogenizing the large composition variations predicted to exist within the main burning zones, these variations are exploited to enlarge the number of possible mixing end-members, and the resulting mixtures are forced to satisfy the constraint that TiC condenses before graphite at equilibrium. For this purpose, compositions of individual layers computed by Rauscher et al. (2002) for supernovae of masses 15, 21 and 25 M_{\odot} are used. These masses are thought to be representative of the stars whose ejecta are likely to have been sampled. Also presented are equilibrium condensation sequences for the bottom, middle and top layer of each of the main burning zones based on layer compositions from the model 21 M_{\odot} supernova. In previous supernova condensation calculations, the variation of total pressure with temperature in the ejecta was considered by Lattimer et al. (1978) and the variation of composition within a zone was considered by Lodders (2006), but the time variation of abundances due to radioactive decay has never been considered. All three effects are included in the present work, a preliminary version of which was presented by Fedkin et al. (2009).

2. TECHNIQUE

Lattimer et al. (1978) constructed density *vs.* temperature profiles for supernova ejecta that are strongly dependent on the initial fraction, f , of the matter that is radioactive. As in Lattimer et al. (1978), we consider the two-step β -decay of ^{56}Ni to be the most important radioactive heat source. In the supernova nucleosynthesis models of Rauscher et al. (2002), an initial ^{56}Ni fraction of $\sim 3 \times 10^{-4}$ was calculated for a 21 M_{\odot} supernova. This value was used to obtain a density-temperature profile for the present work by interpolation between the Lattimer et al. curves. The resulting density-temperature variation was used to obtain a pressure *vs.* temperature variation for each composition used here from the ideal gas law and the mean atomic weight of each bulk composition. Nozawa et al. (2003) computed the density and temperature *vs.* time curves for mixed ejecta at various mass coordinates in a 25 M_{\odot} core-collapse supernova with an initial ^{56}Ni fraction of $\sim 3 \times 10^{-3}$. In the present work, these were used to obtain another temperature *vs.* pressure variation at an interior mass coordinate of 4.6 M_{\odot} using the ideal gas law and the mean atomic weight of each composition. Density and temperature *vs.* time profiles were computed as a function of mass coordinate by Kozasa et al. (in press) for the case of a 15 M_{\odot} core-collapse supernova with an initial ^{56}Ni fraction of $\sim 9 \times 10^{-3}$. A number of these profiles were converted to pressure *vs.* temperature profiles and compared to that of Nozawa et al. (2003) using a constant atomic weight. They were found to cluster around the Nozawa et al. (2003) profile, and the lowest pressure profile so determined from the Kozasa et al. (in press) investigation, the one at a mass coordinate of 1.8 M_{\odot} , was selected for further study in the present work after correcting the pressures for the mean atomic weight of each composition.

Drawing on infrared observations of SN 1987A by [Wooden et al. \(1993\)](#) and optical observations of the Cassiopeia A (Cas A) supernova remnant by [Fesen et al. \(2001\)](#) and [Fesen \(2005\)](#), pressure *vs.* temperature variations are also considered for the case of a supernova with clumpy ejecta. Although at very different stages of evolution, both objects, as well as numerical simulations of core-collapse supernovae, are consistent with explosion of ejecta as dense, homologously expanding clumps, described by [Ouellette et al. \(2010\)](#). When a clump mass $\sim 2 \times 10^{-4} M_{\odot}$ and radius $\sim 1.56 \times 10^{13}$ (t, yr) cm, at the lower limit of optical observations, are assumed, a density $= 4 \times 10^{-10}$ (t, yr) $^{-3}$ g cm $^{-3}$ is obtained. This probably represents an upper limit to the possible densities within the clumps observed in SN 1987A and Cas A, and likely to exist in the ejecta of other core-collapse supernovae.

To derive pressures from the densities, the mean atomic weight of each bulk composition was used, and the dust temperatures were those inferred by [Wooden et al. \(1993\)](#) from infrared observations of optically thick, dusty clumps in SN 1987A, assumed to radiate as blackbodies (their Table 8). These are well described by the formula $T(t) = 3811 - 1214 \log_{10}(t, \text{days})$ K. It is unlikely that the dust in these clumps is in thermal equilibrium with the gas, as most gaseous atomic iron vanished and most dust condensed sometime between days 415 and 615, when dust temperatures dropped below 600 K, well below the condensation temperatures of iron and most silicates. To partially account for this, the gas temperature was set equal to the dust temperature plus 300 K. When this difference was varied from 100 to 500 K, no significant changes in the results of this study were found. For densities based on a mean atomic weight of 16, pressures are inferred to have dropped from $\sim 8 \times 10^{-4}$ bar at day 60, when gas temperatures were

1952 K, to $\sim 7 \times 10^{-8}$ bar at day 777, when temperatures were 602 K. These variations of pressure *vs.* temperature are shown as the top curve of Fig. 1. Because these represent probable upper limits to the density, curves are also shown where the pressure is reduced by factors of 10, 100 and 1000.

Fig. 1 also depicts the profiles derived from [Lattimer et al. \(1978\)](#), [Nozawa et al. \(2003\)](#) and [Kozasa et al. \(in press\)](#). Because of the order of magnitude higher initial ^{56}Ni fraction assumed by [Nozawa et al.](#) and [Kozasa et al.](#), the time to cool from 2000 to 1000 K is ~ 150 days longer than in the Lattimer et al. model. The pressure *vs.* temperature profiles based on the former two studies lie one or two orders of magnitude below the curves based on the Lattimer et al. study. All of the corresponding temperature-time profiles show that cooling of the ejecta occurs on a time-scale comparable to the half-lives of some abundant nuclides; thus, the effect of radioactive decay on elemental abundances is built into the calculations in this paper. The same temperature–time profile was used for every part of the supernova ejecta.

Although nuclidic yields have been computed from other supernova models, *e.g.*, that of [Woosley and Heger \(2007\)](#), the data from [Rauscher et al. \(2002\)](#) are the most accessible. Starting with isotopic abundances calculated by [Rauscher et al.](#) at the 25,000 second mark after the explosion for supernovae with initial masses of 15, 21 and 25 M_{\odot} , the elemental abundances were corrected for radioactive decay using that mark as time-zero for the temperature-time profile in this study. A decay program was built on top of libnucnet, a library for storing and managing nuclear reaction networks ([Meyer and Adams, 2007](#)). In the present work, the decay code was incorporated into the condensation code to enable it to calculate the decay of major radioactive species based on their half-lives, and ultimately to correct elemental abundances at each equilibrium

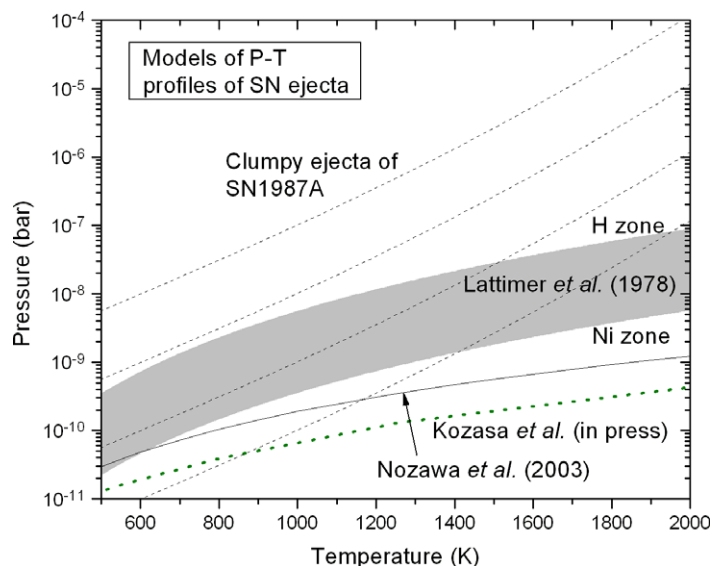


Fig. 1. Pressure–temperature profiles of supernova ejecta used in this work. The profiles derived from [Lattimer et al. \(1978\)](#) are shown as a shaded area between the highest and lowest pressures obtained from the mean atomic weights of the H and Ni zones, respectively. The profile based on [Wooden et al.'s \(1993\)](#) observation of dust clumps in SN1987A is shown for a mean atomic weight of 16, as are curves derived from the latter by reducing the pressures by factors of 10, 100 and 1000 (dashed curves), and those based on [Nozawa et al.'s \(2003\)](#) and [Kozasa et al.'s \(in press\)](#) calculations.

temperature step. The most important radioactive species whose decay influences elemental abundances during condensation are those with half-lives ≤ 2 years, the approximate time needed to cool to 500 K (Wooden et al., 1993). These include 77-day ^{56}Co and 16-day ^{48}V .

Rauscher et al. (2002) computed the nuclidic yields of supernovae of various masses. The present work focuses on their models s15a28c, s21a28g and s25a28d for explosions of stars with initial masses 15, 21 and 25 M_{\odot} , respectively. Rauscher et al. (2002) discretized the compositions of each of their model supernovae into hundreds of relatively thin layers. For the 21 M_{\odot} supernova model, for example, the compositions of 780 layers were computed. These were grouped into the 8 major burning zones of Meyer et al. (1995) in the present work, with most zones containing more than 40 layers. In Fig. 2, the mass fractions of nuclides that define the major burning zones are plotted against distance from the core of the model 21 M_{\odot} supernova, expressed as mass of the star interior to that distance and referred to herein as the internal mass coordinate. Large composition variations exist within some zones in Fig. 2, but differences in nuclidic abundances between adjacent layers within the zones are relatively small. In the present work, the compositions of these thinner layers are considered as potential mixing end-members, instead of the homogenized compositions of the main burning zones considered by Travaglio et al. (1999). In the models for each of the three supernova masses considered here, chemical and isotopic gradients within the ejecta are quite similar, allowing the boundaries between the main burning zones to be defined in the same way in each model. In the present work, it is assumed that the zones within the ejecta of each supernova do not become chemically and isotopically homogenized during the explosion, and that mixing of layers occurs before condensation.

Condensation calculations were carried out using the program of Yoneda and Grossman (1995), whose thermodynamic data set was augmented with gaseous species and solid silicides and titanides that are potentially important in supernova ejecta. Thermodynamic data were taken from Barin (1989) for $\text{FeSi}_{(c)}$ and $\text{FeSi}_{2(c)}$, Knacke et al. (1991) for $\text{NiSi}_{(c)}$, Kubaschewski (1983) for $\text{NiTi}_{(c)}$, $\text{NiTi}_{2(c)}$, $\text{Ni}_3\text{Ti}_{(c)}$, $\text{SiTi}_{(c)}$, $\text{Si}_2\text{Ti}_{(c)}$ and $\text{Si}_3\text{Ti}_{5(c)}$, Kubaschewski and Dench (1955) for $\text{FeTi}_{(c)}$, and from Chase (1998) for additional gaseous species. Conclusions based on the stability of some of the added species, such as Si_3Ti_5 , FeSi_2 , NiTi , SiTi and Si_2Ti , should be treated with caution, as errors on their heats of formation are either not reported or are much larger than for most other crystalline phases in our data base (>25 vs. <2 kJ/mol).

Each condensation calculation is carried out at a specific bulk composition, which is used to convert the density *vs.* temperature curve to a pressure *vs.* temperature curve. The calculation is begun at a time corresponding to a desired initial temperature, which determines the initial total pressure and the proportions of radioactive parents and daughters. Then the temperature is lowered by a preset step size, usually 5 K, where the abundances and total pressure are recalculated, until a preset minimum temperature (1000 K) is reached. It is assumed that chemical equilibrium would not be attainable below this temperature on the short cooling time-scales characteristic of supernova ejecta. The program calculates a series of equilibrium states with the abundances determined at a particular temperature. Fig. 3 is an example of how much radioactive decay can change relative amounts of some abundant elements on the time-scale of cooling of the ejecta. If ^{56}Co condenses, it does so with the chemical properties of cobalt but, after decaying into ^{56}Fe in the condensate, it is allowed to equilibrate with the chemical properties of iron.

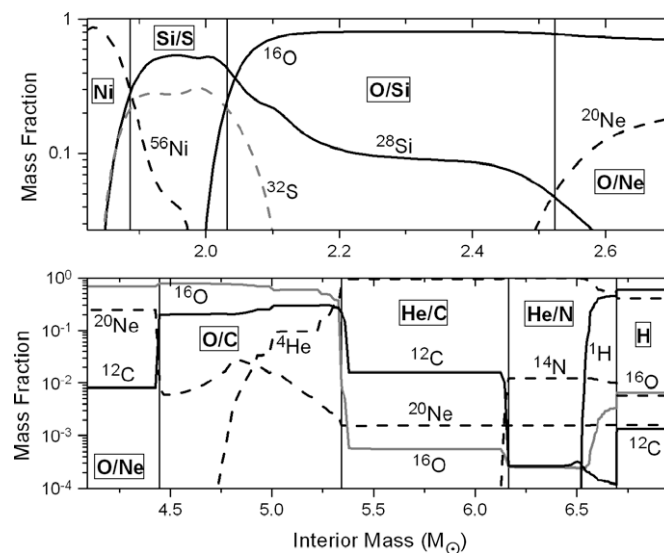


Fig. 2. Mass fractions of the nuclides that define the boundaries (vertical lines) between the eight major burning zones of the 21 M_{\odot} supernova model of Rauscher et al. (2002), plotted against the internal mass coordinate. Note the different *x*- and *y*-axis scales in the upper and lower panels.

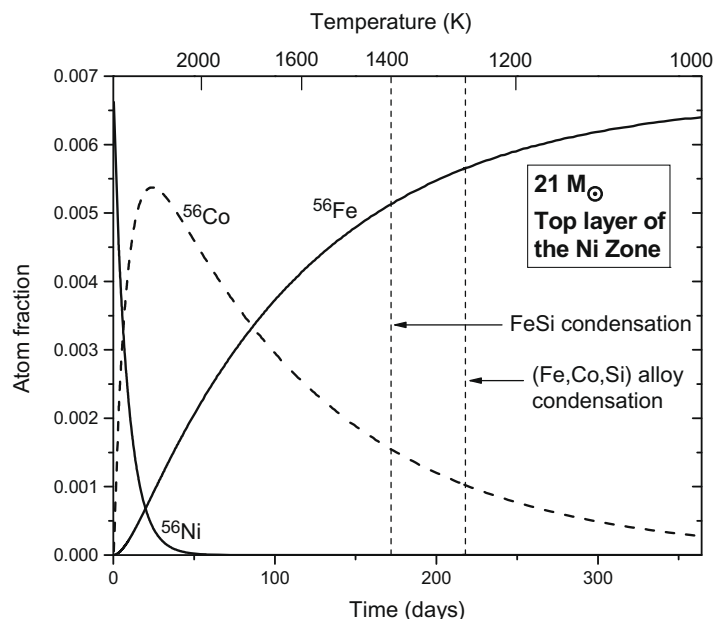


Fig. 3. Variation with time of the atom fractions of ^{56}Ni , ^{56}Co and ^{56}Fe at the top of the Ni zone in the $21 M_{\odot}$ supernova model due to radioactive decay. Shown on the top axis are the temperatures corresponding to the cooling times employed in this work. Initial condensation temperatures of important Fe-containing phases are shown for reference.

3. RESULTS

3.1. Condensation in the $21 M_{\odot}$ supernova model

3.1.1. Condensate phases and sequences

Equilibrium condensation calculations were carried out for many of the individual layer compositions computed by Rauscher et al. (2002) for each of the 15, 21 and $25 M_{\odot}$ supernovae along the pressure–temperature profiles (Fig. 1) derived from Lattimer et al. (1978). While the following discussion, summarized in Table 1, is a detailed description of condensation in specific layers computed by Rauscher et al. (2002) for the $21 M_{\odot}$ model, the similarities in chemical and isotopic gradients between the models for all three supernova masses lead to similar condensate minerals, solid solution compositions, condensation sequences and condensation temperatures at similar relative depths for each supernova mass.

As found by Lattimer et al., condensation temperatures in supernova ejecta are comparable to those in solar gas, despite the much higher pressures assumed for the latter. The reason for this is that, in solar gas, condensable elements are diluted by large amounts of hydrogen, an element that is heavily depleted by nuclear burning in most supernova zones. An exception to this is the outer hydrogen shell, which is very homogeneous in composition due to convection (Meyer et al., 1995). As a result, the condensate assemblage looks similar to that for solar composition throughout the hydrogen shell (Table 1), except that condensation temperatures are generally lower due to the lower pressure. Note that condensation temperatures in this shell would have been even lower had the pre-explosion star been of lower metallicity, *i.e.* formed from interstellar material that is less evolved isotopically, and thus has a lower con-

centration of condensable elements relative to hydrogen than material of solar composition.

The first condensate, corundum (Al_2O_3), condenses at 1480 K, ~ 300 K lower than in 10^{-3} bar solar gas. The composition of the top of the He/N zone is similar to that of the H shell. The condensation temperature of corundum drops with increasing depth within the He/N zone. In the middle of the zone, the condensation temperature of corundum is 100 K lower than at the top, and Ti_2O_3 condenses next, remains stable for 20 K and then reacts with the gas to form perovskite (CaTiO_3). Progressive He burning results in an increase in the carbon abundance with increasing depth within the He/N zone, and the C/O ratio gradually becomes greater than 1. This causes $\text{CO}_{(\text{g})}$ to consume most of the free oxygen, making graphite (C), TiC and SiC the highest-temperature condensates at the base of the He/N zone. On crossing into the He/C zone, a sharp increase in the C/O ratio results in a much higher condensation temperature for graphite (1950–2000 K), followed by TiC (1510 K), SiC (1320 K), Fe and Ni silicides (1090 K) and metal (1065 K). The term “metal” is used in this paper to denote a non-ideal solid solution or alloy of Fe, Ni, Co and Si that is continuously variable in composition, distinct from stoichiometric compounds such as FeSi. AlN and oldhamite (CaS) condense below 1050 K. Production of both ^{12}C and ^{16}O from ^4He burning results in formation of the O/C zone, where oxygen and carbon are the dominant elements. ^{16}O is the most abundant species and the atomic C/O ratio is less than one (Fig. 2) in all three oxygen-rich burning zones (O/C, O/Ne, O/Si), causing oxides such as corundum, grossite (CaAl_4O_7), hibonite ($\text{CaAl}_{12}\text{O}_{19}$) and spinel (MgAl_2O_4) to be the highest-temperature condensates. The decrease in ^{16}O abundance at the bottom of the O/Si zone (Fig. 2) causes the condensation temperature

Table 1

Equilibrium condensation sequences for three different layers in each of the eight major burning zones, from outermost to innermost, in the 21 M_{\odot} supernova model.

Zone	#550*—bottom (6.7 M_{\odot})**		#665—middle (8.2 M_{\odot})		#780—top (14.7 M_{\odot})				
	Tin	Tout	Tin	Tout	Tin	Tout			
H	Corundum	1480	1365	Corundum	1480	1365	Corundum	1480	1365
	Perovskite	1373	1162	Perovskite	1373	1163	Perovskite	1373	1163
	Hibonite	1370	1330	Hibonite	1370	1335	Hibonite	1370	1335
	Grossite	1340	1240	Grossite	1340	1240	Grossite	1340	1240
	CaAl ₂ O ₄	1295	1285	CaAl ₂ O ₄	1295	1285	CaAl ₂ O ₄	1295	1285
	Melilite	1285	1160	Melilite	1285	1160	Melilite	1285	1160
	Hibonite	1240	1183	Hibonite	1240	1183	Hibonite	1240	1183
	Corundum	1183	1180	Corundum	1183	1180	Corundum	1183	1180
	Spinel	1180	1175	Spinel	1180	1175	Spinel	1180	1175
	Plagioclase	1175	1145	Plagioclase	1175	1150	Plagioclase	1175	1150
	Ca-pyroxene	1163	—	Ca-pyroxene	1163	—	Ca-pyroxene	1163	—
	Spinel	1150	1114	Spinel	1150	1115	Spinel	1150	1115
	Olivine	1143	—	Olivine	1145	—	Olivine	1145	—
	Plagioclase	1121	—	Plagioclase	1123	—	Plagioclase	1123	—
	Sphene	1120	—	Sphene	1120	1110	Sphene	1120	1110
	MgTi ₂ O ₅	1110	—	MgTi ₂ O ₅	1110	—	MgTi ₂ O ₅	1110	—
	Opx	1110	—	Opx	1100	—	Opx	1100	—
	Spinel	1095	—	Spinel	1095	—	Spinel	1095	—
Metal	1085	—	Metal	1085	—	Metal	1085	—	
#476—bottom (6.2 M_{\odot})			#505—middle (6.6 M_{\odot})			#549—top (6.7 M_{\odot})			
	Tin	Tout		Tin	Tout		Tin	Tout	
He/N	Graphite	1690	1250	Corundum	1370	1270	Corundum	1470	1360
	TiC	1510	—	Ti ₂ O ₃	1300	1280	Ti ₂ O ₃	—	—
	SiC	1320	1070	Perovskite	1280	1080	Perovskite	1368	1158
	FeSi	1150	—	Hibonite	1270	1230	Hibonite	1360	1320
	Graphite	1090	—	Grossite	1240	1170	Grossite	1330	1230
	NiSi	1080	1060	CaAl ₂ O ₄	1208	1200	CaAl ₂ O ₄	1290	1280
	AlN	1070	—	Melilite	1200	1090	Melilite	1280	1150
	Metal	1060	—	Hibonite	1170	1100	Hibonite	1230	1176
	Oldhamite	1020	—	Spinel	1109	—	Spinel	1176	1170
				Plagioclase	1100	1070	Plagioclase	1170	1140
				Ca-pyroxene	1082	—	Ca-pyroxene	1158	—
				Spinel	—	—	Spinel	1145	1109
				Olivine	1063	—	Olivine	1138	—
				Plagioclase	—	—	Plagioclase	1115	—
				MgTi ₂ O ₅	—	—	MgTi ₂ O ₅	1100	—
				Opx	—	—	Opx	1090	—
				Spinel	—	—	Spinel	1088	—
				Metal	1083	—	Metal	1080	—
			Ti ₂ O ₃	1010	—				
#433—bottom (5.3 M_{\odot})			#454—middle (5.7 M_{\odot})			#475—top (6.1 M_{\odot})			
	Tin	Tout		Tin	Tout		Tin	Tout	
He/C	Graphite	>2000	—	Graphite	1990	—	Graphite	1955	—
	TiC	1510	—	TiC	1510	—	TiC	1510	—
	SiC	1325	1070	SiC	1325	1070	SiC	1320	1070
	FeSi	1090	—	FeSi	1090	—	FeSi	1090	—
	NiSi	1085	1060	NiSi	1080	1060	NiSi	1080	1060
	Metal	1065	—	Metal	1065	—	Metal	1065	—
	Oldhamite	1030	—	AlN	1030	—	AlN	1055	—
	AlN	1005	—	Oldhamite	1025	—	Oldhamite	1025	—
#388—bottom (4.4 M_{\odot})			#409—middle (4.9 M_{\odot})			#432—top (5.3 M_{\odot})			
	Tin	Tout		Tin	Tout		Tin	Tout	
Corundum	1765	1575	Corundum	1760	1580	Corundum	1650	1485	
Grossite	1620	1550	Grossite	1605	1555	Hibonite	1490	1460	

(continued on next page)

Table 1 (continued)

		Tin	Tout		Tin	Tout		Tin	Tout
O/C	Hibonite	1575	1570	Hibonite	—	—	Grossite	1475	1330
	Perovskite	—	—	Perovskite	1580	—	Perovskite	1425	1260
	Spinel	1570	—	Spinel	—	—	Spinel	—	—
	CaAl ₂ O ₄	—	—	CaAl ₂ O ₄	—	—	CaAl ₂ O ₄	1400	1390
	Melilite	1550	1500	Melilite	1555	1504	Melilite	1390	1255
	Olivine	1502	—	Monticellite	1504	—	Hibonite	1330	1305
	Monticellite	1500	—	Olivine	1500	—	Spinel	1310	—
	Periclase	1485	—	Periclase	1495	—	Ca-pyroxene	1260	1215
	Perovskite	1465	—	Perovskite	1475	—	Olivine	1250	—
	Magnetite	1290	1195	Magnetite	1270	1180	Melilite	1219	1200
	Magnesioferrite	1195	—	Magnesioferrite	1180	—	Perovskite	1215	—
	Metal	1105	—	Metal	1115	—	Monticellite	1200	—
						Periclase	1165	—	
						Metal	1070	—	
		#262—bottom (2.5 M _⊙)		#325—middle (3.2 M _⊙)		#387—top (4.4 M _⊙)			
		Tin	Tout	Tin	Tout	Tin	Tout	Tout	
O/Ne	Corundum	1870	1625	Corundum	1855	1613	Corundum	1850	1605
	Grossite	—	—	Grossite	—	—	Grossite	1610	1600
	Spinel	1630	—	Spinel	1613	—	Spinel	1605	—
	Melilite	1600	1555	Melilite	1575	1530	Melilite	1565	1530
	Olivine	1575	—	Olivine	1545	—	Olivine	1533	—
	Ca-pyroxene	1555	1540	Monticellite	1530	—	Monticellite	1530	—
	Plagioclase	1540	—	Periclase	1525	—	Periclase	1520	—
	Opx	1514	—	Perovskite	1460	—	Perovskite	1460	—
	MgTi ₂ O ₅	1385	—	Magnetite	1225	1205	Magnetite	1260	1205
	Sapphirine	1280	—	Magnesioferrite	1205	—	Magnesioferrite	1205	—
	Metal	1115	—	Metal	1105	—	Metal	1105	—
			#213—bottom (2.0 M _⊙)		#237—middle (2.3 M _⊙)		#261—top (2.5 M _⊙)		
		Tin	Tout	Tin	Tout	Tin	Tout	Tout	
O/Si	Grossite	1555	1520	Corundum	1850	1610	Corundum	1870	1625
	Perovskite	1540	1330	Melilite	1616	1590	Spinel	1630	—
	CaAl ₂ O ₄	1520	1505	Spinel	1615	1535	Melilite	1600	1560
	Melilite	1505	1345	Plagioclase	1590	—	Olivine	1575	—
	Larnite	1495	1400	Olivine	1575	1540	Ca-pyroxene	1560	1550
	Rankinite	1400	1370	Opx	1548	—	Plagioclase	1550	—
	Wollastonite	1375	—	Cordierite	1540	—	Opx	1520	—
	Plagioclase	1345	—	Tridymite	1525	—	Cordierite	—	—
	Sphene	1330	1100	Spinel	1470	—	Tridymite	—	—
	Tridymite	1295	—	MgTi ₂ O ₅	1380	1350	Spinel	—	—
	Metal	1170	—	Rutile	1350	—	MgTi ₂ O ₅	1385	—
	Ti ₂ O ₃	1100	—	Metal	1123	—	Sapphirine	1280	—
FeSi	1060	—				Metal	1115	—	
NiSi	1050	—							
TiN	1005	—							
		#199—bottom (1.9 M _⊙)		#205—middle (2.0 M _⊙)		#212—top (2.0 M _⊙)			
		Tin	Tout	Tin	Tout	Tin	Tout	Tout	
Si/S	Si ₃ Ti ₅	1505	1430	Si ₃ Ti ₅	1490	1470	Ti ₂ O ₃	1410	1405
	SiTi	1430	1330	SiTi	1470	—	Perovskite	1405	—
	FeSi	1405	—	FeSi	1405	—	Grossite	1390	1205
	TiC	1350	—	TiC	—	—	Oldhamite	1380	1035
	NiSi	1340	1230	NiSi	1385	—	TiO	1270	1220
	Si ₃ Ti ₅	1330	1155	Si ₃ Ti ₅	—	—	Si ₃ Ti ₅	1220	1115
	Metal	1235	—	Metal	1375	—	FeSi	1200	—
	Oldhamite	1225	—	Oldhamite	1120	—	Grossite	1195	1155
	TiC	1221	1095	TiC	—	—	NiSi	1190	—
	NiSi	1220	—	NiSi	—	—	Melilite	1155	1015
	SiTi	1155	—	SiTi	—	—	SiTi	1115	—

Table 1 (continued)

	Tin	Tout		Tin	Tout		Tin	Tout
	SiC	1095	SiC	1285	—	Metal	1070	—
	TiC	1035	TiC	—	—	Rankinite	1038	1020
						Wollastonite	1020	—
						Grossular	1015	—
						Sinoite	1010	—
	#186—bottom (1.8 M _⊙)		#192—middle (1.8 M _⊙)		#198—top (1.9 M _⊙)			
	Tin	Tout	Tin	Tout	Tin	Tout	Tin	Tout
	Si ₃ Ti ₅	1400	Si ₃ Ti ₅	1350	1285	Si ₃ Ti ₅	1500	1405
	Ni ₃ Ti	1305	Ni ₃ Ti	1289	1260	SiTi	1405	1390
	Metal	1285	Metal	1285	—	FeSi	1400	—
	TiO	1270	TiO	1270	1020	Si ₃ Ti ₅	1390	—
	TiN	1260	TiN	1265	—	TiC	1375	1290
Ni	NiTi	1240	NiTi	1260	1250	Metal	1255	—
	FeTi	1230	FeTi	1250	1130	Oldhamite	1230	—
	Oldhamite	1205	Oldhamite	1190	—	TiC	1080	—
	Ni ₃ Ti	1173	Ni ₃ Ti	1130	—	Al ₂ O ₃	1040	—
	TiC	1115	Hibonite	1025	—			
	Grossite	1035	TiC	1020	—			
	CaAl ₂ O ₄	1015						

Tin—condensation temperature.

Tout—disappearance temperature.

* Layer number, counted from innermost to outermost, from the Rauscher et al. (2002) outputs corresponding to bottom, middle and top of the main burning zones.

** Internal mass coordinate corresponding to the layer number in the Rauscher et al. (2002) outputs.

of the first oxide phase to fall (from ~ 1850 to 1555 K) and makes grossite the first condensate instead of corundum. Because the oxygen abundance continues to fall and that of sulfur increases through the top part of the Si/S zone (Fig. 2), the first condensate (Ti₂O₃) forms at even lower temperature (1410 K) than at the base of the O/Si zone. With falling temperature, Ti₂O₃ is followed by perovskite, grossite and oldhamite. Once ¹⁶O is exhausted in the middle and bottom of the Si/S zone, silicides and titanides (Si₃Ti₅, SiTi, FeSi) become the dominant condensates. Si₃Ti₅ forms at ~ 1500 K at the bottom of the Si/S and top of the Ni zone, followed by SiTi and FeSi. The Si₃Ti₅ condensation temperature falls to 1400 K and those of metal and Ni₃Ti increase slightly at the bottom of the Ni zone as the Si abundance becomes lower due to conversion of Si into Fe-group nuclei in the center of the star.

Table 1 shows that graphite condensation is expected only in the He/C zone and the lowermost He/N zone, while oxides and silicates are the predicted condensates throughout the H, O/C, O/Ne and O/Si zones and the upper part of the He/N zone. Despite the fact that the latter zones collectively represent a much larger fraction of the model supernova's mass than the He/C zone (Fig. 2), there may be kinetic reasons to expect a greater yield of graphite than oxides and silicates from supernovae. Because reaction rates increase with gas pressure and temperature, and condensation occurs while both pressure and temperature are falling rapidly with time, the first phases to condense from any layer are the most likely to form at their equilibrium condensation temperatures shown in Table 1, other things being equal. Note that the phase with the highest

condensation temperature in the He/C zone, graphite, condenses at $T > 1955$ K, considerably higher than the condensation temperature of the earliest phase in almost all of the O-rich zones. For this reason, there may be a greater tendency for subcooling in the O-rich zones, perhaps delaying condensation of oxides and silicates until very low pressures and temperatures are reached, where only amorphous, non-stoichiometric phases, if any, can condense.

3.1.2. Stability and composition of solid solutions

In the H and upper part of the He/N zone, spinel condenses below 1200 K and contains more than 95 mol% MgAl₂O₄. Spinel condenses neither at the base of the He/N nor throughout the He/C zone because the high C/O ratios in those regions preclude formation of oxygen-containing condensates at high temperature. From the bottom of the O/C, and through all of the O/Ne zone to the middle of the O/Si zone, spinel condenses typically above 1600 K. The composition of the first spinel to condense is MgAl₂O₄ and remains so with decreasing temperature in the bottom of the O/C and in the top and middle of the O/Ne zones. In the bottom of the O/Ne and top of the O/Si zones, ~ 20 mol% of MgCr₂O₄ would dissolve in the spinel by 1000 K if equilibrium could be maintained. In the middle of the O/Si zone, spinel first condenses at 1615 K, where it contains 99% MgAl₂O₄, disappears at 1535 K, as condensation of cordierite (Mg₂Al₄Si₅O₁₈) consumes most of the Al, and reappears at 1470 K, where it contains $\sim 45\%$ MgCr₂O₄. The spinel stability field completely disappears toward the bottom of the O/Si zone and throughout the Si/S and Ni zones as the O content falls.

Melilite, a solid solution of gehlenite, Ge, ($\text{Ca}_2\text{Al}_2\text{SiO}_7$) and åkermanite, Åk, ($\text{Ca}_2\text{MgSi}_2\text{O}_7$), is a stable condensate in all of the oxygen-rich zones as well as in the H zone and all but the bottom of the He/N zone. In the H and at the top of the He/N zone, it condenses at ~ 1285 K and disappears at ~ 1160 K, with the mole fraction of åkermanite in the melilite, $X_{\text{Åk}}$, reaching 0.4 with falling temperature. As the C/O ratio rises toward the middle of the He/N zone, the melilite condensation temperature falls from 1285 at the top of the zone to 1200 K in the middle, and the maximum $X_{\text{Åk}}$ falls from 0.4 to 0.05 while the bulk Al/Mg atomic ratio of the zone rises from 0.08 to 0.11. Melilite is not stable above 1000 K at the base of the He/N and throughout the He/C zone because of the high C/O ratios in those zones. In the O/C, O/Ne and O/Si zones, melilite has a high-temperature stability field, usually in the range of 1500–1600 K, with $X_{\text{Åk}}$ rising to 0.64 with decreasing temperature due to consumption of Al by very large amounts of coexisting spinel. Melilite is almost totally absent from both the Ni and Si/S zones.

In the H and He/N zones, plagioclase, a solid solution of anorthite ($\text{CaAl}_2\text{Si}_2\text{O}_8$) and albite ($\text{NaAlSi}_3\text{O}_8$), condenses below 1200 K as pure anorthite but persists for only 30 K. Formation of plagioclase is typical for the O/Si and the bottom of the O/Ne zones, where it condenses above 1500 K as pure anorthite. If equilibrium could be maintained, the albite content would increase to 94 mol% by 1000 K at the top of the O/Si zone, as the bulk Na/Ca atomic ratio is ~ 3.7 . Ca-rich pyroxene is stable in the H zone below 1163 K, where it condenses within 10 K of plagioclase and is mostly diopside ($\text{CaMgSi}_2\text{O}_6$, >70 mol%) with ~ 20 mol% kushiroite ($\text{CaAl}_2\text{SiO}_6$) and 10 mol% $\text{CaTiAl}_2\text{O}_6$. It has narrow stability fields (<20 K) at the boundary between the O/Ne and O/Si zones, where its composition is also dominated by diopside, with 17 mol% kushiroite. It contains very little Ti because the bulk Ti/Mg ratio of these regions is only $\sim 6 \times 10^{-5}$.

Olivine is a solid solution of forsterite, Fo, (Mg_2SiO_4) and fayalite, Fa, (Fe_2SiO_4); and orthopyroxene a solid solution of enstatite, En, (MgSiO_3) and ferrosilite, Fs, (FeSiO_3). The compositions of the H envelope and He/N zone are close to solar and therefore are quite reducing, so the equilibrium X_{Fa} of the olivine and X_{Fs} of the orthopyroxene do not exceed 0.002 above 1000 K, despite the relatively high atomic Fe/Mg ratio of these zones (0.84). Olivine that appears in the O-rich zones, usually between 1500 and 1600 K, is forsterite with X_{Fa} varying between 0 and 0.03. Despite the abundant oxygen in those zones ($\log f_{\text{O}_2} \sim \text{IW} + 3$), the very low atomic Fe/Mg ratio, $\sim 2 \times 10^{-3}$, precludes a significant fayalite content in the olivine. Orthopyroxene, forming at about the same temperature but after olivine, in these zones is pure enstatite for the same reason. In the Ni and Si/S zones, however, where Fe is one of the most abundant elements, the oxygen fugacity is so low ($\log f_{\text{O}_2} < \text{IW} - 20$) that silicates are not stable at all. Without mixing of materials from different parts of the ejecta, there is no way to make very fayalitic olivine in supernovae. Messenger et al. (2005) used condensation calculations to show that fayalitic olivine is stable in an oxygen-rich mixture of materials from different supernova zones.

Metal is a stable phase in all of the supernova zones, its composition depending on the bulk composition of the zone. It usually appears at a relatively low temperature (<1100 K) except for the deepest layers of the Si/S and Ni zones (1235–1375 K) where Si and Fe-group elements are abundant. In the H and most of the He/N zone, metal is a binary FeNi alloy with a Ni content up to 25 mol%. In the He/C zone, the FeNi alloy becomes rich in silicon (up to 22 mol%) because of the very low oxygen fugacity ($\log f_{\text{O}_2} \sim \text{IW} - 27$). In contrast, the O-rich zones are so oxidizing that the metal alloys are not only free of Si but they also contain very little Fe due to oxidation of the latter. As a result, the metal contains >90 mol% Ni, and FeO condenses into abundant olivine, orthopyroxene and/or magnesioferrite (MgFe_2O_4). Between the middle of the O/Si zone and its base, $\log f_{\text{O}_2}$ falls precipitously from $\text{IW} + 2.7$ to $\text{IW} - 5$, causing the metal to change its composition drastically from >90 mol% Ni to ~ 90 mol% Fe. The abrupt decrease in oxygen and increase in silicon contents from the O/Si to the Si/S zone result in formation of metal containing 80 mol% Si at the top of the Si/S zone. As the silicon abundance rises from the top toward the middle of the zone, the condensation temperature of metal increases to 1375 K and its initial Si content rises to 99%. The abundance of silicon decreases and that of ^{56}Ni increases in the bottom of the Si/S zone. The ^{56}Ni fully decays into ^{56}Co by the time metal condenses, resulting in metal with a high initial cobalt content (67 mol%). Eventually, the ^{56}Co decays into iron, which forms the more stable silicide, enriching the residual metal in silicon. As the silicon abundance falls and that of ^{56}Ni rises further toward the middle of the Ni zone, silicides become less stable, and the initially Fe-, Ni-, Co-rich alloy becomes more Fe-rich with falling temperature.

4. DISCUSSION

4.1. Mixtures required for matching isotopic ratios

4.1.1. Mixing of material from Ni- and C-rich zones

The observation of presolar graphite containing abundant inclusions of TiC suggests that TiC condensed earlier, and therefore at a higher temperature, than graphite. Excesses of ^{28}Si and ^{44}Ca from the decay of short-lived ^{44}Ti associated with this assemblage can only be produced in the inner Ni or Si/S zones of the supernova ejecta. Graphite formation, however, is only possible in the outer, C-rich, He/C and He/N zones. Thus, equilibrium condensation of TiC and graphite with these isotopic characteristics requires mixing of layers from these two widely separated parts of the supernova. Astronomical observations of the Cas A supernova remnant show knots of inner, Fe-rich matter mixed out beyond the layers that experienced oxygen burning (e.g., Hughes et al., 2000), suggesting that the required mixing might occur.

Detailed calculations show how such mixing likely occurs (e.g., Kifonidis et al., 2003; Hammer et al., 2010). Strong convective overturn in post-shock layers of the star leads to significant asphericity in the explosion. As the shock reaches composition boundaries in the progenitor

star, the shock's asphericity seeds Rayleigh–Taylor instabilities. Fingers of inner core material reach into the outer layers and fragment into clumps, or bullets, that travel faster than their local environment. In 2-d simulations (Kifonidis et al., 2003), the shock slows considerably as it passes through the He/H interface, causing the He-rich zone to pile up in a dense “wall”. Metal clumps that penetrate into this wall slow down and eventually co-move with the He-rich material. This scenario could ultimately lead to microscopic mixing between ^{44}Ti -rich core material and He/C zone matter. In 3-d simulations (Hammer et al., 2010), “bullets” of “nickel”-rich (where, by “nickel”, Hammer et al. mean elements with $Z > 8$) and oxygen-rich matter form with high velocities. The fastest nickel bullets in fact overtake the oxygen bullets, and both nickel and oxygen bullets penetrate the He-rich zones. The fastest can reach into the H envelope. As Hammer et al. (2010) conclude, the original onion-skin structure of the star is at least partially overturned.

Graphite is the first condensate in the He/C zone, followed by TiC. Mixing of any layer from that zone with more and more material from the Ni zone builds up the Ti abundance, ultimately resulting in a reversal of the condensation sequence, with TiC condensing at a higher temperature than graphite. Most of the Ti in the Ni zone is ^{44}Ti and ^{48}Ti . The initial concentration of the latter is negligible but becomes significant as a result of radioactive decay ($^{48}\text{Cr} \rightarrow ^{48}\text{V} \rightarrow ^{48}\text{Ti}$) by the time condensation begins. The top layer of the Ni zone was selected as a mixing end-member because it contains high abundances of ^{28}Si and ^{44}Ti . In addition, another layer from near the bottom of the Ni zone, the same ^{44}Ti -rich one for all mixtures from the same supernova mass, was selected in amounts sufficient to match the highest observed $^{26}\text{Al}/^{27}\text{Al}$ ratios, which are discussed later. For the 15, 21 and 25 M_{\odot} supernova mod-

els considered in this work, at least twice as much total material from the Ni zone as from the He/C zone is required for condensation of TiC ahead of graphite. As seen in Table 2, the ratios of material from these layers that are used in all ejecta mixtures discussed in the remainder of this paper guarantee that TiC always condenses at a higher temperature than graphite.

4.1.2. Carbon and nitrogen isotopic compositions

The observed graphite grains are characterized by a large range of $^{12}\text{C}/^{13}\text{C}$, with most of the values plotting between 6 and 1300, and excesses in ^{15}N relative to ^{14}N of up to a factor of 10 relative to solar (Fig. 4a). The He/C zone is very rich in ^{12}C relative to ^{13}C ($^{12}\text{C}/^{13}\text{C} \sim 2.3 \times 10^3 - 2.0 \times 10^5$) and the Ni zone contains very little carbon. In order to match the $^{12}\text{C}/^{13}\text{C}$ ratios of the graphite spherules, admixture of relatively ^{13}C -rich He/N zone material is necessary. The He/N zone, however, has high $^{14}\text{N}/^{15}\text{N}$ ratios relative to the solar value, making it difficult to find a match that would satisfy both $^{12}\text{C}/^{13}\text{C}$ and $^{14}\text{N}/^{15}\text{N}$ ratios simultaneously.

Travaglio et al. (1999) discussed the problem of possible N isotopic equilibration of the graphite grains. They pointed out that it was not clear where equilibration occurred but, assuming the compositions with which the grains equilibrated were normal, the measured $^{14}\text{N}/^{15}\text{N}$ ratios would be lower limits to the original ratios if the latter were larger than normal, and upper limits if smaller than normal. As seen in Fig. 4a, most of the measured $^{14}\text{N}/^{15}\text{N}$ values are smaller than the solar ratio (272), meaning that the data may reflect only upper limits to the original ratios of the graphite, if Travaglio et al. (1999) are correct. In this case, fitting the presumed original compositions (having even lower $^{14}\text{N}/^{15}\text{N}$ values than shown in Fig. 4a at the same $^{12}\text{C}/^{13}\text{C}$ ratios) by mixing He/C zone material with

Table 2
Mixing ratio ranges of layers selected from the major burning zones.

Rauscher et al. (2002) models:	s15a28c	s21a28g	s25a28d
Initial mass	15 M_{\odot}	21 M_{\odot}	25 M_{\odot}
Upper Ni zone layer #	369 (1.8 M_{\odot})	198 (1.9 M_{\odot})	226 (2.2 M_{\odot})
lower Ni zone layer #	346 (1.7 M_{\odot})	189 (1.8 M_{\odot})	215 (2.1 M_{\odot})
O/Ne zone layer #	440 (2.2 M_{\odot})	262 (2.5 M_{\odot})	329 (3.3 M_{\odot})
He/N zone layer #	691 (4.1 M_{\odot})	494 (6.5 M_{\odot})	589 (8.3 M_{\odot})
Lower Ni:upper Ni	0–1.4	0–4	0–6.7
Ni:He/C*	10–150	2–40	2–50
He/N:He/C	0.5–60	0.2–2	0.1–3
He/C:O/Ne	≥ 10	25–100	≥ 50
Results			
TiC before graphite?	Yes	Yes	Yes
C/O	1.4–12.6	1.2–3.6	1.3–17.8
$^{12}\text{C}/^{13}\text{C}$	17–1358	138–1358	87–1358
$^{14}\text{N}/^{15}\text{N}$	53–403	134–403	75–403
$^{16}\text{O}/^{18}\text{O}$	15–226	4–12	8–137
$^{26}\text{Al}/^{27}\text{Al}$	0.005–0.14	0.01–0.13	0.004–0.13
$^{44}\text{Ti}/^{48}\text{Ti}$	0.05–0.17	0.04–0.26	0.05–0.29
$\delta^{46}\text{Ti}/^{48}\text{Ti}$	–986 to –988	–990 to –995	–989 to –994
$\delta^{49}\text{Ti}/^{48}\text{Ti}$	–440 to –640	–484 to –805	–477 to –805
$\delta^{29}\text{Si}$	–970 to –980	–960 to –980	–880 to –970

* For each supernova mass, the specific layer selected from the He/C zone varied.

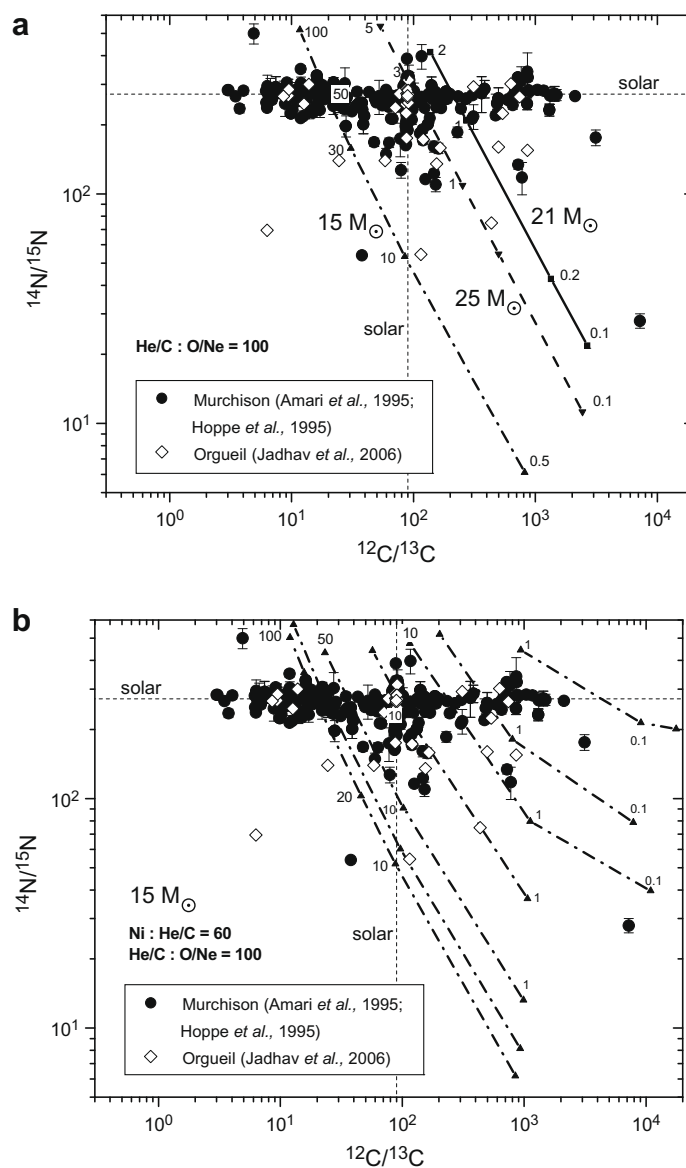


Fig. 4. Carbon and nitrogen isotopic compositions of mixtures of ejecta layers from supernovae whose compositions were calculated by Rauscher et al. (2002), compared to isotopic compositions measured in low-density graphite spherules. The numbers along the curves are the mass ratios of material from a middle layer of the He/N zone to that from the layer of the He/C zone in the mixtures, whose compositions were obtained by varying the amount of material from the layer of the He/N zone. The mass ratios of material from the Ni zone to that from the layer of the He/C zone to that from the bottom layer of the O/Ne zone are fixed at 60:1:0.01, 8:1:0.01 and 15:1:0.01 for the 15, 21 and 25 M_{\odot} models, respectively. Dashed vertical and horizontal lines indicate solar isotopic ratios. (a) Isotopic compositions of representative mixtures of layers that yield good agreement with the isotopic data and also allow condensation of TiC at a higher temperature than graphite along the profiles in Fig. 1 derived from Lattimer et al. (1978), for each of the 15, 21 and 25 M_{\odot} supernova models. (b) The ranges of carbon and nitrogen isotopic compositions that can be generated by selecting different layers from the bottom part of the He/C zone to add to the mixture in the 15 M_{\odot} supernova model, while also allowing condensation of TiC before graphite. The series of curves is generated simply by using a different layer of the He/C zone as a mixing end-member, from Layer #601 of Rauscher et al. (2002) to Layer #620, separated by 0.26 M_{\odot} , in the direction of increasing $^{14}\text{N}/^{15}\text{N}$ ratio. (See above-mentioned references for further information.)

He/N zone material would be even more difficult. In an attempt to satisfy both $^{12}\text{C}/^{13}\text{C}$ and $^{14}\text{N}/^{15}\text{N}$ ratios simultaneously, Travaglio et al. (1999) assumed that only a small fraction of the ^{14}N in the He/N zone was incorporated into the grains, or that production of ^{15}N in the He/C zone was much higher than in the 15 M_{\odot} supernova model used by them, that of Woosley and Weaver (1995). This was only

partially successful, as it was quite difficult to match low $^{14}\text{N}/^{15}\text{N}$ ratios at subsolar $^{12}\text{C}/^{13}\text{C}$ ratios.

Use of specific, individual layers from the major burning zones as mixing end-members can potentially overcome this problem. Except for mixtures illustrated in Fig. 4b, the layer of the He/C zone with the lowest $^{14}\text{N}/^{15}\text{N}$ ratio (near the bottom of the He/C zone) and the layer of the He/N

zone with the highest ^{13}C mass fraction (near the middle of the He/N zone) were selected for mixing from the model compositions of Rauscher et al. (2002) for each of the 15, 21 and 25 M_{\odot} supernovae. When the layers are selected in this way, the one from the He/C zone always has a higher $^{12}\text{C}/^{13}\text{C}$ ratio and a lower $^{14}\text{N}/^{15}\text{N}$ ratio than the layer of the He/N zone. While holding the mass ratios of material from the Ni zone to that from the He/C zone to that from the bottom layer of the O/Ne zone fixed at 60:1:0.01, 8:1:0.01 and 15:1:0.01 for the 15, 21 and 25 M_{\odot} models, respectively, varying the amount of material from the He/N zone that is added to the above mixtures creates an inverse correlation between $^{14}\text{N}/^{15}\text{N}$ and $^{12}\text{C}/^{13}\text{C}$ ratios for each supernova mass. As seen in Fig. 4a, each line crosses the field of the measured data points at a different place and extends to lower $^{14}\text{N}/^{15}\text{N}$ ratios, where the original compositions of the graphite may have been. If the ratio of material from the He/N zone to that from the He/C zone had been varied by varying the amount of material from the He/C zone instead, similar isotopic agreement would have been obtained but excursions in the C/O ratio would have been created. In some instances, these excursions would have precluded formation of TiC and graphite (for $\text{C}/\text{O} < 1$) and, in others, would have inverted the equilibrium condensation sequence of TiC and graphite (for $\text{C}/\text{O} \gg 1$), unless offsetting adjustments were made to the relative amount of material from the O/Ne zone.

Because the ^{12}C mass fraction is very nearly the same and that of ^{13}C is negligible in almost all layers of the He/C zone for a given supernova mass, creating mixtures by selecting different layers from the bottom half of the He/C zone, that have higher $^{14}\text{N}/^{15}\text{N}$ ratios than the layer selected in the previous paragraph, produces a family of curves that is shifted upward relative to the line for the same mass in Fig. 4a. This is illustrated for the 15 M_{\odot} supernova in Fig. 4b. Of the three supernova models considered in this work, the mixtures in the 15 M_{\odot} model have

the lowest $^{12}\text{C}/^{13}\text{C}$ ratio at any given $^{14}\text{N}/^{15}\text{N}$ ratio, so generating mixtures using various layers of the He/C zone in this model covers the widest range of observed $^{12}\text{C}/^{13}\text{C}$ ratios (20–8000) while simultaneously matching the $^{14}\text{N}/^{15}\text{N}$ ratios. Because of the ability to account for the low $^{14}\text{N}/^{15}\text{N}$ ratios observed in the graphite spherules with sub-solar $^{12}\text{C}/^{13}\text{C}$ ratios, this study represents a significant improvement over the work of Travaglio et al. (1999).

4.1.3. Oxygen isotopic compositions

Oxygen and carbon isotopic ratios measured in bulk spherules are shown in Fig. 5. The $^{16}\text{O}/^{18}\text{O}$ ratios vary from 3 to 700. Stadermann et al. (2005) found that the $^{16}\text{O}/^{18}\text{O}$ ratio of a graphite spherule from Murchison varies from just over 200 in its core to just over 300 at its rim, *i.e.* becomes more normal toward its outside, suggesting that these objects may have been contaminated with isotopically normal oxygen. Because of this finding, ratios in the upper half of the distribution were considered to be the most contaminated with normal oxygen, and mixing calculations focused on fitting the $^{16}\text{O}/^{18}\text{O}$ ratios in the lower half. The mixtures of material from the Ni, He/C and He/N zones described above contain too little ^{16}O to match the $^{16}\text{O}/^{18}\text{O}$ ratios of the spherules. An ^{16}O -rich layer from any of the O/Si, O/Ne or O/C zones must be added to increase the $^{16}\text{O}/^{18}\text{O}$ ratio of the mixture. The bottom layer of the O/Ne zone was selected. In order to maintain a C/O ratio high enough to ensure that both TiC and graphite are stable at high temperature, however, the amount of this material must be kept low, a constraint that automatically limits the maximum $^{16}\text{O}/^{18}\text{O}$ ratio to the lower portion of the range preserved in the graphite spherules. The mixtures from the 15 and 25 M_{\odot} models found above to give the best fit to the carbon and nitrogen isotopic compositions are consistent with $^{16}\text{O}/^{18}\text{O}$ ratios of ~ 30 –100, while those from the 21 M_{\odot} model have $^{16}\text{O}/^{18}\text{O}$ ratios consistent with the lowest ratios observed in the spherules (Fig. 5).

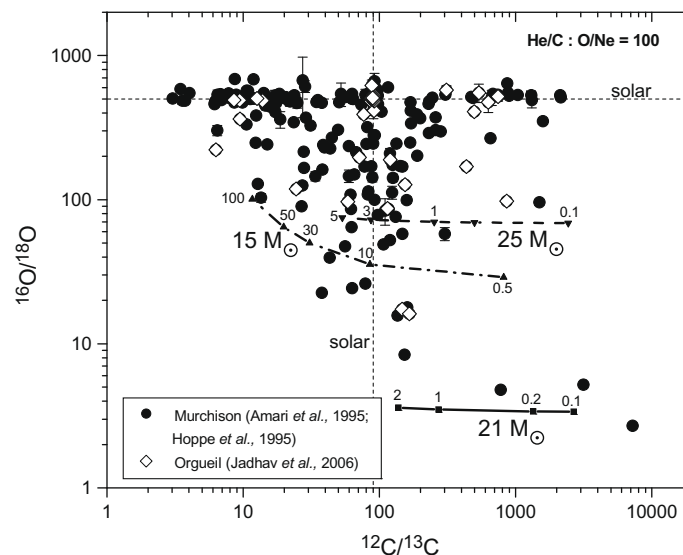


Fig. 5. Oxygen and carbon isotopic ratios of the same mixtures as in Fig. 4a, compared to those measured in the low-density graphite spherules. Labels are the same as in Fig. 4. (See above-mentioned references for further information.)

This difference is due to the fact that the layer of the He/C zone selected for the mixture in the 21 M_{\odot} model, the layer with the lowest $^{14}\text{N}/^{15}\text{N}$ ratio, has an $^{16}\text{O}/^{18}\text{O}$ ratio <1 for this supernova mass, whereas it has $^{16}\text{O}/^{18}\text{O}$ ratios >1 for the others. This, in turn, is due to less ^{18}O destruction during explosive nucleosynthesis in the 21 M_{\odot} model than in those for the other two masses.

4.1.4. Initial $^{26}\text{Al}/^{27}\text{Al}$ ratios

The inferred initial $^{26}\text{Al}/^{27}\text{Al}$ ratios of the spherules range from 10^{-5} to ~ 0.14 . Jadhav et al. (2010) suggested that low-density graphite spherules may have undergone equilibration with normal magnesium. Accordingly, modeling efforts in the present work focused on fitting the highest of the observed $^{26}\text{Al}/^{27}\text{Al}$ ratios. In the mixtures discussed above, the main contributors of ^{26}Al and ^{27}Al are the two layers from the Ni zone. Due to a shift from α -rich to α -poor freeze-out with increasing height within the Ni zone of all three supernova masses, the $^{26}\text{Al}/^{27}\text{Al}$ ratio is very high, ~ 1.5 – 2.4 , in the innermost layers and much lower, ~ 1 – 2×10^{-3} , in the outer layers. Thus, matter from both the topmost layer of the Ni zone and a lower layer had to be used to create mixtures with $^{26}\text{Al}/^{27}\text{Al}$ ratios $>\sim 10^{-3}$. In order to hold the $^{26}\text{Al}/^{27}\text{Al}$ ratio to ≤ 0.14 , the ratio of material from the top layer to that from the lower layer has to be ≥ 0.15 . As seen in Fig. 6, the mixtures found above to give the best fit to the carbon, nitrogen and oxygen isotopic compositions can account for the highest observed $^{26}\text{Al}/^{27}\text{Al}$ ratios.

4.1.5. Silicon isotopic compositions

The mixtures found above to give the best matches to the carbon, nitrogen, oxygen and aluminum isotopic compositions give poor fits to the observed silicon isotopic com-

positions. While $\delta^{29}\text{Si}$ and $\delta^{30}\text{Si}$ observed in the graphite spherules both range from -400‰ to $+400\text{‰}$, most spherules have $\delta^{29}\text{Si}$ and $\delta^{30}\text{Si}$ from -400‰ to zero. The possibility exists that some of these samples were contaminated with normal silicon, which would imply that the original δ -values were even lower. The model mixtures yield very large negative values, $<-900\text{‰}$. This is a consequence of selecting large amounts of the top layer of the Ni zone, which has an overwhelming abundance of ^{28}Si relative to ^{29}Si and ^{30}Si , and a lower layer of the Ni zone having only a small Si mass fraction, in order to match the $^{26}\text{Al}/^{27}\text{Al}$ ratios.

4.1.6. Titanium isotopic compositions

Travaglio et al. (1999) showed that the inferred initial $^{44}\text{Ti}/^{48}\text{Ti}$ ratios of the low-density graphite spherules range from 10^{-3} to 10^{-1} , and that most of them have normal $\delta^{46}\text{Ti}/^{48}\text{Ti}$ and $\delta^{47}\text{Ti}/^{48}\text{Ti}$ with large excesses of ^{49}Ti ($\delta^{49}\text{Ti}/^{48}\text{Ti}$ from several hundred to 10^3) and smaller excesses of ^{50}Ti . The relatively large ratio of matter from the Ni zone to that from the He/C zone required for TiC to condense at a higher temperature than graphite cannot match these Ti isotopic compositions, as very large negative values of $\delta^{46}\text{Ti}/^{48}\text{Ti}$, $\delta^{47}\text{Ti}/^{48}\text{Ti}$, $\delta^{49}\text{Ti}/^{48}\text{Ti}$ and $\delta^{50}\text{Ti}/^{48}\text{Ti}$ are produced (Table 2). These negative anomalies gradually disappear as the ratio of Ni zone matter to He/C zone matter falls by a factor of 10^4 , but the $^{44}\text{Ti}/^{48}\text{Ti}$ ratios remain in the range of 10^{-2} to 10^{-1} . This suggests that a match to the Ti isotopic compositions of the grains might be found by accepting lower proportions of Ni zone matter, and relaxing the constraint that TiC must condense at a higher temperature than graphite. Although the $^{46}\text{Ti}/^{48}\text{Ti}$ and $^{47}\text{Ti}/^{48}\text{Ti}$ ratios become normal when the ratio of Ni zone matter to He/C zone matter is in the range of 10^{-4} to

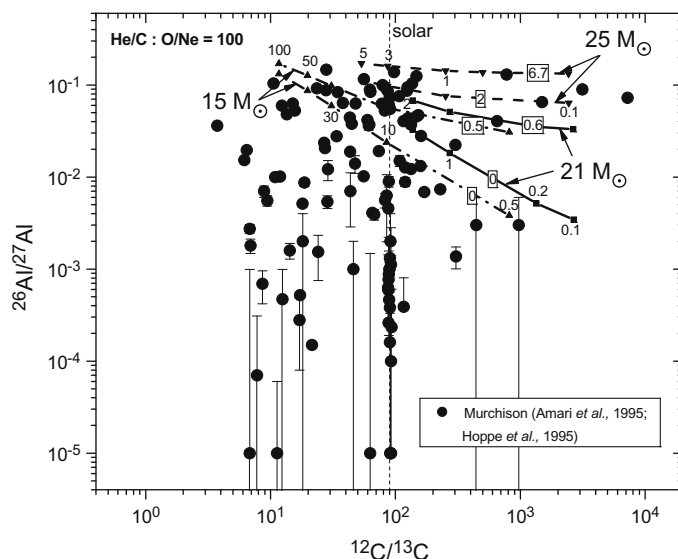


Fig. 6. Aluminum and carbon isotopic compositions of the same mixtures as in Fig. 4a, compared to those measured in the low-density graphite spherules. Modeling efforts focused on matching only the highest $^{26}\text{Al}/^{27}\text{Al}$ ratios, as the grains may have been equilibrated with normal magnesium (Jadhav et al., 2010). For each supernova mass, two curves are shown for different ratios of matter from a lower layer of the Ni zone to that from the topmost layer of the Ni zone, and labeled by the numbers in squares. Other labels are the same as in Fig. 4. (See above-mentioned references for further information.)

10^{-3} , there are two problems with this. The first is that, for such mixtures, $\delta^{49}\text{Ti}/^{48}\text{Ti}$ and $\delta^{50}\text{Ti}/^{48}\text{Ti}$ are $\sim 5000\%$, or 5–10 times larger than observed. The second problem is that $\delta^{29}\text{Si}/^{28}\text{Si}$ and $\delta^{30}\text{Si}/^{28}\text{Si}$ of the mixtures are ~ 1400 and $\sim 2200\%$, respectively, while most of the graphite grains have excess ^{28}Si . When material from the Si/S zone, amounting to ~ 38 times the mass of that from the Ni zone, is added to this mix, graphite condenses at a higher temperature than TiC, the $^{26}\text{Al}/^{27}\text{Al}$ ratio is not altered very much, $\delta^{46}\text{Ti}/^{48}\text{Ti}$ and $\delta^{47}\text{Ti}/^{48}\text{Ti}$ become normal, and $\delta^{29}\text{Si}$ and $\delta^{30}\text{Si}$ become ~ -700 and $\sim -600\%$, all similar to values observed in the spherules. In this mixture, however, $\delta^{49}\text{Ti}/^{48}\text{Ti}$ and $\delta^{50}\text{Ti}/^{48}\text{Ti}$ are $\sim 4700\%$ and $\sim 4300\%$, respectively, both much higher than observed. It appears that, whenever material from the deepest zones of the supernova is mixed with He/C zone material, it is very difficult to match both the Ti and Si isotopic compositions of the graphite spherules, regardless of the condensation sequence. This may point to inadequacies in the treatment of nucleosynthesis in the innermost regions of the star. For example, the [Rauscher et al. \(2002\)](#) stellar evolution and explosion models are one-dimensional. Perhaps multidimensional effects lead to different conditions in the pre-supernova star or its explosion and, thereby, to somewhat different Ti and/or Si nucleosynthetic yields. It is also possible that some nuclear reaction rates are not correct. These issues are worth addressing in the future.

4.1.7. Range of permissible mixtures

It has been shown herein that specific proportions of matter from the Ni zone, a layer near the bottom of the He/C zone and the bottom layer of the O/Ne zone, when added in varying proportions to matter from a layer near the middle of the He/N zone in each of the 15, 21 and 25 M_{\odot} supernova models, yield mixtures whose carbon, nitrogen, oxygen and aluminum isotopic compositions overlap those observed in the graphite spherules and whose chemical compositions cause TiC to condense at a higher temperature than graphite at equilibrium. Those specific proportions can be varied, however. The top of [Table 2](#) shows the ranges of mass ratios of the same layers used above for each of the supernova models, which produce acceptable matches to the required chemical and observed isotopic parameters. The bottom of [Table 2](#) shows the ranges of those parameters generated by the mass ratios at the top of the Table. In some cases on the Table, a different layer from the He/C zone was selected than the one used for the Figures in this work. If less matter from the Ni zone were added to the mix in proportion to that from the He/C zone than the proportions shown on the Table for each supernova mass, graphite would condense at a higher temperature than TiC at equilibrium; if more material from the Ni zone were added than the proportions shown, both TiC and SiC would condense at a higher temperature than graphite. Keeping the ratio of matter from the layer of the He/N zone to that from the He/C zone within the ranges shown on the Table ensures reasonable matches to the carbon and nitrogen isotopic data. If the amount of matter from the O/Ne zone were varied such that the ratio of matter from the layer of the He/C zone

to that from the O/Ne zone were lower or higher than the ranges shown in the Table, then either the C/O ratio would be < 1 , and neither TiC nor graphite would condense; or the model $^{16}\text{O}/^{18}\text{O}$ ratios would be too low relative to the ratios observed in the graphite spherules, respectively.

The Table does not include all possible mixtures that would fit the data, as different but nearby layers could be selected from any or all of the zones than the ones used for the Table, and they would provide acceptable matches. In general, however, the ranges of mixing ratios that would meet the chemical and isotopic constraints would be narrower for the alternative layers than for the layers selected in this work.

4.1.8. Isotopic compositions of other elements

[Table E1](#), available in the electronic annex, presents relative abundances for all nuclides through $Z = 30$, including many elements not discussed above, in the mixtures by the time the temperature falls to 1000 K, equivalent to approximately 1 year of decay after the explosion. The Table gives relative nuclidic abundances for one specific mixture within the range for each model supernova mass in the top of [Table 2](#).

4.1.9. Pressure effects

The isotopic compositions of the low-density graphite spherules necessitate mixing of supernova layers from inner and outer zones. Because different pressure–temperature profiles may result in different condensation sequences, calculations were also performed at higher and lower pressures than those considered by [Lattimer et al. \(1978\)](#). To illustrate the effect of pressure on the condensation sequence, one of the mixtures from the 21 M_{\odot} model that gave a satisfactory fit to the carbon, nitrogen, oxygen and aluminum isotopic compositions was selected. [Fig. 7](#) shows the condensation sequence for all profiles derived from those in [Fig. 1](#), identified by their pressures at 2000 K. The profile derived from the [Kozasa et al.](#) study lies at the low-pressure end and the profile obtained from clumpiness of the ejecta at the high-pressure end. As is the case for all mixtures discussed above, TiC is the highest-temperature condensate and is followed by graphite, along the pressure–temperature profiles derived from the [Lattimer et al. \(1978\)](#), [Nozawa et al. \(2003\)](#) and [Kozasa et al. \(in press\)](#) studies shown in [Fig. 1](#). After graphite forms in these three profiles, the sequence of condensation with declining temperature is SiC, FeSi and metal. The condensation sequence along the [Lattimer et al. \(1978\)](#) profile of [Fig. 1](#) is very similar to the one shown on [Fig. 7](#) for the [Kozasa et al. \(in press\)](#) profile, except that condensation temperatures are all displaced to temperatures ~ 80 K higher. Above a total pressure of $\sim 2 \times 10^{-6}$ bar (at 2000 K), TiC is still the highest temperature condensate but SiC also condenses at a higher temperature than graphite, driving the condensation temperature of the latter to below those of FeSi and metal alloy. Under these conditions, SiC condenses at a lower temperature than TiC and at a higher temperature than graphite. Metal is stable only at low temperature (< 1360 K) for the low-pressure profiles ($< 10^{-7}$ bar at 2000 K); however, its condensation temperature begins to rise more steeply with

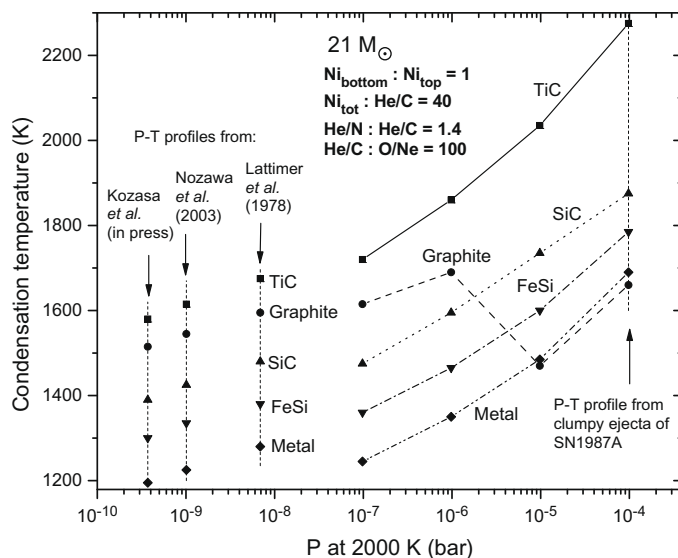


Fig. 7. Equilibrium condensation sequences calculated for one of the mixtures of layers from the $21 M_{\odot}$ supernova model considered in this work. The mean atomic weight of this mixture was used to derive a pressure *vs.* temperature curve from each of the density *vs.* temperature curves taken from Lattimer et al. (1978), Nozawa et al. (2003) and Kozasa et al. (in press), as well as those derived from modeling the clumpiness of the ejecta from SN1987A.

increasing pressure, particularly above 10^{-5} bar, where its condensation temperature lies between those of FeSi and graphite (Fig. 7).

4.1.10. The FeNi metal grains

TiC inclusions found within graphite spherules in Murchison (Croat et al., 2003) indicate that condensation of graphite must follow that of TiC. Croat et al. (2003) also observed tiny metal grains epitaxially attached to TiC grains within the graphite spherules. The metal grains are much less abundant than TiC and are not always observed with the latter. The textures suggest that metal formed after TiC and later became overgrown by graphite. This sequence could be explained by condensation at total pressures $> \sim 10^{-5}$ bar at 2000 K (Fig. 7) except that, under these conditions, SiC and FeSi also condense at a lower temperature than TiC and at a higher temperature than graphite. As a result, equilibrium condensation calculations for relatively high pressures predict that FeSi and SiC inclusions should also be found in graphite. Inclusions of SiC have been found only rarely (Croat et al., 2009) and FeSi not at all. Furthermore, the predicted abundance of metal is much larger, by a factor of ~ 80 , than the abundance of TiC, rather than the reverse, and the calculated composition of the metal is very Si-rich ($\text{Fe}_{56}\text{Si}_{35}\text{Ni}_7\text{CO}_2$), while that described by Croat et al. (2003) is mostly Fe, usually with $< 10\%$ Ni.

To account for the metal textures, Lodders (2006) suggested that $(\text{Fe,Ni})_2\text{Ti}$ grains condensed at the base of the Ni zone, and were ejected into the outer, C-rich, He/C zone where they were incorporated by condensing graphite with which they later reacted to form TiC and (Fe,Ni) . Because Lodders (2006) calculated that phases such as Ti_5Si_3 , $(\text{Fe,Ni})\text{Si}$ and CaS would condense at higher temperature than $(\text{Fe,Ni})_2\text{Ti}$ in the Ni zone and because none of these three

phases are seen as inclusions in the graphite, she theorized that nearly complete silicon-burning must have reduced the abundances of silicon and sulfur by a factor of 1000, so that $(\text{Fe,Ni})_2\text{Ti}$ would become the highest-temperature condensate. This model requires more energetic conditions in the Ni zone than in any of the Rauscher et al. (2002) models used here, and is not without problems. First, it relies on thermodynamic data for Fe_2Ti , which are highly uncertain due to incomplete formation of this phase during its calorimetric measurement (Kubaschewski and Dench, 1955). Second, the ^{28}Si excesses measured in the low-density graphite must still be accounted for, but the ^{28}Si abundance in an otherwise important reservoir of this isotope has been reduced by a factor of 10^3 in this model. Because of the likely impact of these highly energetic conditions on chemical and isotopic compositions throughout the supernova, it is not known whether mixing of ejecta layers in such an object would be capable of generating systems having the carbon, nitrogen, oxygen and silicon isotopic compositions observed in the graphite, and in which the latter phase is the highest-temperature condensate. In the event that such systems can be created in the Lodders (2006) model, it is likely that mixing of gaseous constituents from different depths within the supernova would still be required to do so.

In the present study, the only regions of the supernova where binary alloys of Ni and Fe form are in the outer H and He/N zones. Adding gaseous material from these zones to the mixtures discussed above would not only destroy the isotopic matches to the observed data but would also add significant Si to the resulting condensate metal alloys. Although grains of binary NiFe alloys that condensed from an outer zone could conceivably have been mechanically incorporated by parcels of matter consisting of the gaseous mixtures discussed herein before graphite condensed

from those parcels, the alloy grains would have been accompanied by many other condensate phases from those same outer zones (Table 1), which are not observed as inclusions in the graphite. Also investigated in the present work were mixtures of layers from the He/C zone and the inner part of the Ni zone in an attempt to find compositions capable of condensing TiC and NiFe alloys at a higher temperature than graphite, but this always led to very large proportions of metal compared to TiC, rather than the reverse, which is observed.

5. CONCLUSIONS

At all total pressures, TiC has a higher equilibrium condensation temperature than graphite in all mixtures employed in this work, in agreement with textural observations. This is a more stringent constraint than the one used by Travaglio et al. (1999), $C/O = 1$, which does not guarantee this condensation sequence. In the Rauscher et al. (2002) model compositions of ejecta from 15, 21 and 25 M_{\odot} supernovae, specific layers were found within the main Ni, O/Ne, He/C and He/N zones that, when mixed together, simultaneously match the carbon, nitrogen and oxygen isotopic compositions as well as the $^{44}\text{Ti}/^{48}\text{Ti}$ ratios and the inferred initial $^{26}\text{Al}/^{27}\text{Al}$ ratios of the low-density graphite spherules. Of the three supernova masses, the mixtures of layers from the 15 M_{\odot} model supernova cover the widest range of $^{12}\text{C}/^{13}\text{C}$ ratios (20–8000) while simultaneously matching the $^{14}\text{N}/^{15}\text{N}$ ratios. This is a significant improvement over the previous attempt, as Travaglio et al. (1999) were unable to match the nitrogen isotopic compositions of the spherules at $^{12}\text{C}/^{13}\text{C}$ ratios <100 . In the mixtures for all supernova masses, successful matches to the initial $^{26}\text{Al}/^{27}\text{Al}$ ratios were obtained by selection of two layers from the Ni zone, the topmost layer and a lower layer. This allowed fitting of $^{26}\text{Al}/^{27}\text{Al}$ ratios as low as 10^{-2} at $^{12}\text{C}/^{13}\text{C}$ ratios as low as 10^2 , also a significant improvement over the work of Travaglio et al. (1999), who were unable to reach such $^{26}\text{Al}/^{27}\text{Al}$ ratios at $^{12}\text{C}/^{13}\text{C}$ ratios below 10^4 . Due to the relatively large proportion of material from the Ni zone required for the equilibrium condensation temperature of TiC to be higher than that of graphite, and the relative amounts of the two layers of the Ni zone required to match the initial $^{26}\text{Al}/^{27}\text{Al}$ ratios, the predicted silicon isotopic compositions are more ^{28}Si -rich than observed in the low-density graphite. The relatively large amount of Ni zone material also produces large negative $\delta^{46}\text{Ti}/^{48}\text{Ti}$, $\delta^{47}\text{Ti}/^{48}\text{Ti}$, $\delta^{49}\text{Ti}/^{48}\text{Ti}$ and $\delta^{50}\text{Ti}/^{48}\text{Ti}$, which contrast with the near-normal $\delta^{46}\text{Ti}/^{48}\text{Ti}$ and $\delta^{47}\text{Ti}/^{48}\text{Ti}$, large positive $\delta^{49}\text{Ti}/^{48}\text{Ti}$ and smaller positive $\delta^{50}\text{Ti}/^{48}\text{Ti}$ characteristic of the graphite spherules. Although better matches to the observed $\delta^{46}\text{Ti}/^{48}\text{Ti}$, $\delta^{47}\text{Ti}/^{48}\text{Ti}$ and ^{28}Si excesses can be found by making mixtures from much smaller amounts of Ni zone material and some material from the Si/S zone, it is very difficult to simultaneously match the Ti and Si isotopic compositions in any mixtures of material from these deep layers with He/C and He/N zone material, regardless of the condensation sequence. The occurrence of Fe-rich, Si-poor metal grains inside the graphite spherules does not yet have a satisfactory explanation.

ACKNOWLEDGMENTS

We thank T. Bernatowicz, T. Croat, S. J. Desch, C. Ellinger, R. Gallino, S. B. Simon and E. Zinner for helpful discussions. This paper benefitted greatly from reviews by E. Zinner, M. Petaev and an anonymous reviewer. This work was supported by funds from the National Aeronautics and Space Administration through Grants NNG05GG00G (to L.G.) and NNX07AJ04G (to B.S.M.).

APPENDIX A. SUPPLEMENTARY DATA

Supplementary data associated with this article can be found, in the online version, at doi:10.1016/j.gca.2010.03.021.

REFERENCES

- Amari S. and Zinner E. (1997) Supernova grains from meteorites. In *Astrophysical Implications of the Laboratory Study of Presolar Materials* (eds. T. J. Bernatowicz and E. Zinner), AIP Conf. Proc. **402**, pp. 287–305.
- Amari S., Zinner E. and Lewis R. S. (1995) Large ^{18}O excesses in circumstellar graphite grains from the Murchison meteorite: indications of a massive-star origin. *Astrophys. J.* **447**, L147–L150.
- Amari S., Zinner E. and Lewis R. S. (1996) ^{41}Ca in presolar graphite of supernova origin. *Astrophys. J.* **470**, L101–L104.
- Barin I. (1989) *Thermochemical Data of Pure Substances*. VCH, Weinheim.
- Bernatowicz T. J., Amari S., Messenger S. and Lewis R. S. (1998) Internal structure and composition of presolar graphites from supernovae. *Lunar Planet. Sci. XXIX*. Lunar Planet. Inst., Houston. #1393 (abstr.).
- Bernatowicz T. J., Bradley J., Amari S., Messenger S. and Lewis R. S. (1999) New kinds of massive star condensates in a presolar graphite from Murchison. *Lunar Planet. Sci. XXX*. Lunar Planet. Inst., Houston. #1392 (abstr.).
- Chase M. W. Jr. (1998) NIST-JANAF Thermochemical Tables. Fourth Edition. *J. Phys. Chem. Ref. Data, Monograph 9*. American Institute of Physics, Woodbury, New York.
- Cherchneff I. and Dwek E. (2009) The chemistry of Population III supernova ejecta. I. Formation of molecules in the early universe. *Astrophys. J.* **703**, 642–661.
- Clayton D. D., Liu W. and Dalgarno A. (1999) Condensation of carbon in radioactive supernova gas. *Science* **283**, 1290–1292.
- Croat T. K., Bernatowicz T., Amari S., Messenger S. and Stadermann F. J. (2003) Structural, chemical, and isotopic microanalytical investigations of graphite from supernovae. *Geochim. Cosmochim. Acta* **67**, 4705–4725.
- Croat T. K., Jadhav M., Lebsack E. and Bernatowicz T. J. (2009) Low-density presolar graphite spherules from the Orgueil meteorite. *Lunar Planet. Sci. XL*. Lunar Planet. Inst., Houston. #2175 (abstr.).
- Ebel D. S. and Grossman L. (2001) Condensation from supernova gas made of free atoms. *Geochim. Cosmochim. Acta* **65**, 469–477.
- Fedkin A. V., Meyer B. S., Grossman L. and Desch S. J. (2009) Condensation in supernova ejecta at high spatial resolution. *Lunar Planet. Sci. XL*. Lunar Planet. Inst., Houston. #1699 (abstr.).
- Fesen R. A. (2005) Recent X-ray, optical, and near-infrared observations of supernova remnants. In *1604–2004: Supernovae as Cosmological Lighthouses* (eds. M. Turatto, S. Benetti, L. Zampieri and W. Shea), ASP Conf. Series 342, pp. 409–415.

- Fesen R. A., Morse J. A., Chevalier R. A., Borkowski K. J., Gerardy C. L., Lawrence S. S. and Van den Bergh S. (2001) Hubble Space Telescope WFPC2 imaging of Cassiopeia A. *Astrophys. J.* **122**, 2644–2661.
- Hammer N. J., Janka H.-T. and Müller E. (2010) Three-dimensional simulations of mixing instabilities in supernova explosions. eprint arXiv:0908.3474.
- Hoppe P., Amari S., Zinner E. and Lewis R. S. (1995) Isotopic compositions of C, N, O, Mg, and Si, trace element abundances, and morphologies of single circumstellar graphite grains in four density fractions from the Murchison meteorite. *Geochim. Cosmochim. Acta* **59**, 4029–4056.
- Hughes J. P., Rakowski C. E., Burrows D. N. and Slane P. O. (2000) Nucleosynthesis and mixing in Cassiopeia A. *Astrophys. J.* **528**, L109–L113.
- Jadhav M., Amari S., Zinner E. and Maruoka T. (2006) Isotopic analysis of presolar graphite grains from Orgueil. *New Astron. Rev.* **50**, 591–595.
- Jadhav M., Amari S., Zinner E. and Maruoka T. (2010) Presolar graphite grains from Orgueil: Some unresolved issues. *Lunar Planet. Sci. XLI*. Lunar Planet. Inst., Houston. #1035 (abstr.).
- Kifonidis K., Plewa T., Janka H.-T. and Müller E. (2003) Non-spherical core collapse supernovae. I. Neutrino-driven convection, Rayleigh–Taylor instabilities, and the formation and propagation of metal clumps. *Astron. Astrophys.* **408**, 621–649.
- Knacke O., Kubaschewski O. and Hesselmann K. (1991) *Thermochemical Properties of Inorganic Substances*, second ed. Springer, Berlin.
- Kozasa T., Nozawa T., Tominaga N., Umeda H., Maeda K. and Nomoto K. (in press) Dust in supernovae: Formation and evolution. In *Cosmic Dust-Near and Far* (eds. Th. Henning, E. Grün and J. Steinacker), ASP Conf. Series.
- Kubaschewski O. (1983) Thermochemical properties. In *Titanium: Physico-chemical Properties of its Compounds and Alloys* (ed. K. L. Komarek), Atomic Energy Review Spec. Issue 9, International Atomic Energy Agency, Vienna, pp. 1–71.
- Kubaschewski O. and Dench W. A. (1955) The heats of formation in the systems titanium–aluminium and titanium–iron. *Acta Metall.* **3**, 339–346.
- Lattimer J. M., Schramm D. N. and Grossman L. (1978) Condensation in supernova ejecta and isotopic anomalies in meteorites. *Astrophys. J.* **219**, 230–249.
- Lodders K. (2006) They came from the deep in the supernova: the origin of TiC and metal subgrains in presolar graphite grains. *Astrophys. J.* **647**, L37–L40.
- Messenger S., Keller L. P. and Lauretta D. S. (2005) Supernova olivine from cometary dust. *Science* **309**, 737–741.
- Meyer B. S. and Adams D. C. (2007) Libnucnet: a tool for understanding nucleosynthesis. *Meteoritics Planet. Sci. Supp.*, **42**, #5215 (abstr.).
- Meyer B. S., Weaver T. A. and Woosley S. E. (1995) Isotope source table for a 25 M_⊙ supernova. *Meteoritics* **30**, 325–334.
- Nittler L. R., Amari S., Zinner E., Woosley S. E. and Lewis R. S. (1996) Extinct ⁴⁴Ti in presolar graphite and SiC: proof of a supernova origin. *Astrophys. J.* **462**, L31–L34.
- Nittler L. R., Alexander C. M. O'D., Gallino R., Hoppe P., Nguyen A. N., Stadermann F. J. and Zinner E. K. (2008) Aluminum-, calcium- and titanium-rich oxide stardust in ordinary chondrite meteorites. *Astrophys. J.* **682**, 1450–1478.
- Nozawa T., Kozasa T., Umeda H., Maeda K. and Nomoto K. (2003) Dust in the early universe: dust formation in the ejecta of population III supernovae. *Astrophys. J.* **598**, 785–803.
- Ouellette N., Desch S. J. and Hester J. J. (2010) Injection of supernova dust in nearby protoplanetary disks. *Astrophys. J.* **711**, 597–612.
- Rauscher T., Heger A., Hoffman R. D. and Woosley S. E. (2002) Nucleosynthesis in massive stars with improved nuclear and stellar physics. *Astrophys. J.* **576**, 323–348.
- Sharp C. M. and Wasserburg G. J. (1995) Molecular equilibria and condensation temperatures in carbon-rich gases. *Geochim. Cosmochim. Acta* **59**, 1633–1652.
- Stadermann F. J., Croat T. K., Bernatowicz T. J., Amari S., Messenger S., Walker R. M. and Zinner E. (2005) Supernova graphite in the NanoSIMS: carbon, oxygen and titanium isotopic compositions of a spherule and its TiC sub-components. *Geochim. Cosmochim. Acta* **69**, 177–188.
- Travaglio C., Gallino R., Amari S., Zinner E., Woosley S. E. and Lewis R. S. (1999) Low-density graphite grains and mixing in Type II supernovae. *Astrophys. J.* **510**, 325–354.
- Wooden D. H., Rank D. M., Bregman J. D., Witterborn F. C., Tielens A. G. G. M., Cohen M., Pinto P. A. and Axelrod T. S. (1993) Airborn spectrophotometry of SN 1987A from 1.7 to 12.6 microns: History of the dust continuum and line emission. *Astrophys. J. Supp.* **88**, 477–507.
- Woosley S. E. and Heger A. (2007) Nucleosynthesis and remnants in massive stars of solar metallicity. *Phys. Repts.* **442**, 269–283.
- Woosley S. E. and Weaver T. A. (1995) The evolution and explosion of massive stars. II. Explosive hydrodynamics and nucleosynthesis. *Astrophys. J. Supp.* **101**, 181–235.
- Yoneda S. and Grossman L. (1995) Condensation of CaO–MgO–Al₂O₃–SiO₂ liquids from cosmic gases. *Geochim. Cosmochim. Acta* **59**, 3413–3444.

Associate editor: Jitendra N. Goswami